



# Enhanced visible light photocatalytic activity of alkaline earth metal ions-doped CdSe/rGO photocatalysts synthesized by hydrothermal method



Mingjun Zhou<sup>a</sup>, Donglai Han<sup>b,c</sup>, Xinlin Liu<sup>a</sup>, Changchang Ma<sup>d</sup>, Huiqin Wang<sup>d</sup>, Yanfeng Tang<sup>a</sup>, Pengwei Huo<sup>a,\*</sup>, Weidong Shi<sup>a,\*</sup>, Yongsheng Yan<sup>a</sup>, Jinghai Yang<sup>c</sup>

<sup>a</sup> School of Chemistry & Chemical Engineering, Jiangsu University, Zhenjiang 212013, PR China

<sup>b</sup> Changchun Institute of Optics, Fine Mechanics and Physics, Chinese Academy of Sciences, Changchun 130033, PR China

<sup>c</sup> Key Laboratory of Functional Materials Physics and Chemistry of the Ministry of Education, Jilin Normal University, Siping 136000, PR China

<sup>d</sup> School of Environment, Jiangsu University, Zhenjiang 212013, PR China

## ARTICLE INFO

### Article history:

Received 7 November 2014

Received in revised form

23 December 2014

Accepted 5 January 2015

Available online 15 January 2015

### Keywords:

QDs CdSe

Alkaline earth metal ions

Reduced graphene oxide

Hydrothermal method

## ABSTRACT

Quantum dots (QDs) CdSe exhibits relatively high photocatalytic abilities for its unique properties, but the aggregation and photocorrosion have blocked its further application. Therefore, for arriving at a solution, alkaline earth metal ions ( $M = Mg^{2+}$ ,  $Ca^{2+}$ ,  $Sr^{2+}$  and  $Ba^{2+}$ ) and reduced graphene oxide (rGO) are chosen to fabricated new QDs CdSe-based photocatalytic systems. In this paper,  $M@CdSe/rGO$  composites have been synthesized via a facile one-step hydrothermal approach, during which the formation of  $M$  doped CdSe crystallization and GO reduction occur simultaneously. The obtained photocatalysts demonstrates synergistically enhanced visible light photocatalytic activity and stability toward photodegrading tetracycline hydrochloride (TC-HCl) solution, especially the introduction of 6 mol%  $Ca^{2+}$  and 5 wt% GO on QDs CdSe resulted in 85.6% degradation of 15 mg/L TC-HCl in 1 h with 0.5 g/L catalyst. Furthermore, the photodegradation mechanism was systematically investigated by active species trapping experiment. It revealed that  $h^+$  was the major active species in the destructions process. And the possible process of charge transfer for  $Ca^{2+}@CdSe/rGO$  nanocomposite was proposed based on the experimental results.

© 2015 Elsevier B.V. All rights reserved.

## 1. Introduction

Semiconductor nanomaterials for removal of toxic pollutants and dealing with energy crisis have becoming a hot topic over the world [1]. Common semiconductors such as  $TiO_2$ ,  $WO_3$  and  $ZnO$  have been previously reported for their better optical and photocatalytic performances. As we all known, the photogenerated electrons ( $e^-$ ) and holes ( $h^+$ ) will be produced from the semiconductors under visible or ultraviolet light irradiation. Photogenerated  $e^-$  transfers from valence band (VB) to the conduction band (CB) with  $h^+$  leaving in the valence band (VB) and the  $e^-/h^+$  pairs play an important role in producing active species during the photodegradation process [2]. However, the fast recombination of charge carriers generated from photocatalytic reactions would weaken the photocatalytic activity of these semiconductors. Thus, recently various strategies have been taken to deal

with these problems, such as doping with ions [3], coupling with narrow band-gap semiconductors [4] or loading on the carbon materials [5] and the sensitizing treatment [6]. The common carbon-based nanomaterials such as carbon nanotubes, graphene oxide (GO) and carbon nitride have been investigated to be the effective architectures for the highly efficient charge collection and separation. Among all the carbon-based nanomaterials, the lamellar structure of rGO bestows remarkable and unique properties, such as high specific surface area, large spring constants, high chemical, a high mobility of charge carriers [7] and electrochemical stability [8], which has been regarded as ideal guest component for fabricating rGO-based functional materials [9]. On account of its favorable properties, rGO has been utilized in thermomechanics, chemistry, photology and electrochemically [10], and also provides new opportunities for photocatalyst carriers or promoter. Hence, great interests have been focused on the synthesis of rGO/semiconductors with GO as the raw material by sufficiently exerting the excellent electron conductivity of rGO to lengthen the lifetime of photoexcited charge carriers in the semiconductor [11]. Besides, as a support to deposit and

\* Corresponding authors. Tel.: +86 511 8879 0187; fax: +86 511 8879 1800.

E-mail address: [huopw@mail.ujs.edu.cn](mailto:huopw@mail.ujs.edu.cn) (P. Huo).

stabilize semiconductors, rGO can also act as synergist to promote the charge separation, restrain the  $e^-/h^+$  recombination and improve the electron capture-storage-transport properties of the compound nanomaterials [12], which results in an enhanced photocatalytic activity. Enhanced photocatalysis has been previously reported of rGO-mediated photocatalysts such as  $TiO_2/rGO$ ,  $CdS/rGO$  and  $Ag/rGO$  [13–15]. Recently, research works focused on methods to employ rGO to modify  $CdX$  ( $X = S, Se, Te$ ) quantum dots (QDs) show an enhanced visible-light photocatalytic activities.

Quantum dots (QDs) applied in the degradation of environmental contaminations under visible-light irradiation have generalized widely attention by researchers for their unique properties such as quantum size effect [16], quantum confinement effect [17], advantageous optical properties [18], multiple exciton generation effect [19] and size-dependent optical and electronic properties, processing versatility and low cost [14]. As the traditional II–VI semiconductor nanomaterial, QDs CdSe with the narrow band gap energy  $E_g = 1.75$  eV is regarded as a promising visible-light photocatalyst, which is sensitive to visible light and has been widely applied in photodegradation of organic pollutants, solar cell, photoluminescence [20], etc. However, there are still several issues that limit the utilization of pure QDs CdSe nanoparticles. For example, QDs CdSe nanoparticles are prone to aggregation, resulting in a reduced surface area and the high recombination rate of photogenerated  $e^-/h^+$  pairs is another problem to restrict its wide application. Photogenerated electrons in QDs farther away from the wide band gap semiconductor must efficiently complete a greater number electron transfer hopping events without undergoing recombination or trapped-state termination [21]. Therefore, discovering novel methods to improve the photocatalytic performance of QDs CdSe are still the hotspot research. Herein, combining QDs CdSe with rGO can not only act as a support to highly disperse and stabilize CdSe nanoparticles [22], but also serve as a new type of promising photocatalyst for environmental amelioration. Lotfi and Saboohi [23] reported QDs CdSe loading on graphene nanocomposites exhibited excellent photocatalytic activity on degrading malachite green. Liu et al. [5] also reported graphene-based QDs CdSe photocatalysts displayed great catalytic and optical properties in photodegrading rhodamine B and industrial dye. The increasing migration ability of the photocatalysts after modification with rGO can leads to the formation of strong heterojunction electric field on the interface between rGO and the inorganic semiconductor material for the difference in their Fermi levels [24]. After coupling with rGO, an interfacial electric field is established at the interface, which efficiently enhanced the separation of electron–hole pairs. The electrons transferred to the rGO through the interface between these two materials and participate in reduction reactions by dissolved oxygen occurring on the surface of rGO, while the holes leaving from the VB of the semiconductor materials can either react with the adsorbed water to form hydroxyl radicals or oxidize the pollutants directly [25]. Even though, QDs with rGO modification have facilitated the electrons and holes separation, the active recombination reaction of  $e^-/h^+$  pairs still occurs inside the QDs. The possible strategies toward this problem can be included to change the QDs noumenal properties such as changing the spacing between CB and VB of QDs or produce the impurity energy level inside the QDs. In that case, doping with metal ions can be the effective methods to realize this strategy.

It has been reported that, the recombination of  $e^-/h^+$  pairs could be separated by hybridizing QDs CdSe with metallic ions, such as doping transition-metal ions  $Mn^{2+}@CdSe$  [26] for better visible-light absorption. Photoinduced  $e^-/h^+$  pairs can be separated efficiently by the Schottky barrier formed on the interface of compound CdSe-based semiconductor [27], for improving the photocatalytic activities. Due to the good ability of electron-donating and stability of alkaline-earth metal ions, especially the ionic

radius is similar to Cd ion. QDs CdSe modification with doping alkaline-earth metal ions may be a possible method to reduce the recombination of  $e^-/h^+$  pairs. Common alkaline-earth metal ions like  $Mg^{2+}$ ,  $Ca^{2+}$ ,  $Sr^{2+}$ ,  $Ba^{2+}$  with good stability and charge transition properties have rarely been applied in modifying semiconductor. Meanwhile, how the doped alkaline earth metal ions effect on the photocatalytic properties of the CdSe-based materials have not demonstrated completely by previous reports. Therefore, the investigation on the mechanism of alkaline metal ions, doping will be beneficial for the future semiconductor modification [28].

Herein, we reported a novel  $M@CdSe/rGO$  ( $M = Mg^{2+}$ ,  $Ca^{2+}$ ,  $Sr^{2+}$ ,  $Ba^{2+}$ ) composite nanoparticles by one step method through hydrothermal method for utilization of photodegrading TC-HCl under visible-light irradiation. The characteristics of obtained samples were studied by transmission electron microscopy (TEM), high resolution transmission electron microscopy (HRTEM) images, selected area electron diffraction (SAED), X-ray diffraction (XRD), energy dispersive X-ray (EDX) analysis, UV-vis diffuse reflectance spectroscopy (DRS), Raman spectroscopy, X-ray photoelectron spectroscopy (XPS), photoluminescence (PL) spectra. The photocatalytic properties were obtained by photodegrading TC-HCl solution and the absorbance datum and spectra were observed by UV-vis spectrophotometer. In addition, the stability and mechanism of the composites during photodegrading TC-HCl were attentively studied.

## 2. Experimental

### 2.1. Chemicals and reagents

Graphite powder, sodium nitrate ( $NaNO_3$ , AR), potassium permanganate ( $KMnO_4$ , AR), sulfuric acid ( $H_2SO_4$ , AR), magnesium chloride hexahydrate ( $MgCl_2 \cdot 6H_2O$ , AR), strontium chloride hexahydrate ( $SrCl_2 \cdot 6H_2O$ , AR), barium chloride dehydrate ( $BaCl_2 \cdot 2H_2O$ , AR), calcium chloride ( $CaCl_2$ , CP) and hydrochloric acid (HCl, AR) were purchased from Sinopharm Chemical Reagent Co., Ltd. Hydrogen peroxide ( $H_2O_2$ , 30%), 3-mercaptopropionic acid (MPA, 98%) were obtained from Aladdin Chemistry Co., Ltd. Cadmium chloride hydrate ( $CdCl_2 \cdot 2.5H_2O$ , AR), sodium hydroxide (NaOH, AR), benzoquinone (BQ, AR), ethanol (AR), triethanolamine (TEOA, AR), isopropanol (IPA, AR) and methanol were all purchased from Shanghai Chemical Reagent Co., Ltd., and used as received. Tetracycline hydrochloride was obtained from Shanghai Shunbo Biological Engineering Co., Ltd.

### 2.2. Samples preparation

#### 2.2.1. Preparation of GO

Graphene oxide (GO) was synthesized through liquid oxidation according to the modified Hummers method [29,30]. Typically, 30 mL  $H_2SO_4$  containing 1 g graphite powder and 2.5 g  $NaNO_3$  was mixed in a 250 mL three necked flask, followed by stirring treatment at 0 °C to obtain a homogeneous suspension. Then, 4 g  $KMnO_4$  was dissolved in above mixture for 2 h until the mixture turned green. When the temperature climbed to 35 °C, 40 mL  $H_2O$  was then added. The reaction mixture was stirred at 98 °C for 40 min. After the solution turns golden, 10 mL  $H_2O_2$  and 40 mL  $H_2O$  were added to terminate the reaction, respectively. Then the solution was collected through precipitation and centrifugation, washed thoroughly with 30% HCl, and dried in vacuum at 60 °C for 12 h.

#### 2.2.2. Preparation of alkaline-earth metals ions $M@CdSe/rGO$

Quantum dots (QDs) CdSe were synthesized via a hydrothermal method according to the literature reported by Rogach and Kornowski [31].  $M@CdSe/rGO$  nanoparticles were prepared as follows: 0.09134 g  $CdCl_2 \cdot 2.5H_2O$  and desired amount of alkaline-earth

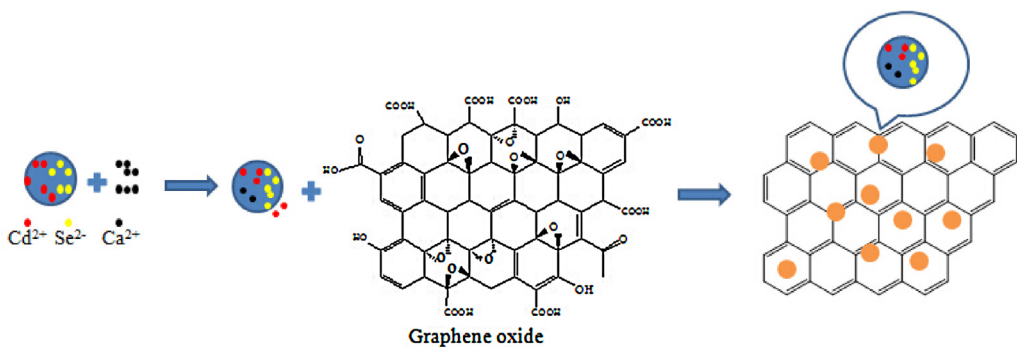


**Fig. 1.** The schematic illustration on formation of  $\text{Ca}^{2+}$ @CdSe/rGO compound photocatalyst.

metals ions ( $M$ ) (2, 4, 6, 8, 10 mol%) were added into a 50 mL beaker dissolving with 30 mL deionized water, respectively. Four types of alkaline-earth metals,  $\text{MgCl}_2 \cdot 6\text{H}_2\text{O}$ ,  $\text{CaCl}_2$ ,  $\text{SrCl}_2 \cdot 6\text{H}_2\text{O}$ , and  $\text{BaCl}_2 \cdot 2\text{H}_2\text{O}$ , were used as the dopants. Then, a solution of 0.056 mL 3-mercaptopropionic acid serving as the stabilizing agent was added with stirring for 5 min. After that, the pH was regulated at a level of 9 by 1 mol NaOH and then followed by adding GO (1, 3, 5, 7, 9%). Meanwhile, 0.0592 g Se powders mixed with 0.3783 g sodium borohydride in a 20 mL round bottom flask and then added with 5 mL deionized water stirring under nitrogen atmosphere until the transparent sol was obtained. When the solution turns clear with white precipitate appeared, the clear liquid was quickly injected into the above solution. After stirring the resulting mixture for 15 min at room temperature to obtain a homogeneous suspension, this suspension was subject to hydrothermal treatment at 160 °C for 40 min. The final products  $M@\text{CdSe}/\text{rGO}$  were obtained by centrifugation and drying at 60 °C for 12 h. During this hydrothermal treatment, the reduction of GO to rGO and the deposition treatment can be simultaneously achieved [32]. The obtained nanoparticles were treated by centrifugation, washed by water, and fully dried at 60 °C in oven to get the final nanocomposites. The preparation process is illustrated in Fig. 1.

### 2.3. Characterization

The transmission electron microscopy (TEM), high-resolution transmission electron microscopy (HRTEM) images, and selected area electron diffraction (SAED) were examined by transmission electron microscopy (TEM: JEM-2010, Japan). Energy dispersive X-ray spectroscopy (EDS) was recorded on a FEI Tecnai G2F20 instrument and operated at an accelerating voltage of 200 kV. The crystal phase was carried out by powder X-ray diffraction (XRD), which is obtained by X-ray diffractometer (MAC Science, Japan) equipped with Ni-filtrated Cu K $\alpha$  radiation (40 kV, 30 mA). The  $2\theta$  scanning angle range was 5–80° at a scanning rate of 5° min<sup>-1</sup>. The optical properties of the samples were analyzed by UV-vis diffuse reflectance spectroscopy (DRS) with a specord 2450 spectrometer (Shimazu, Japan) in the wavelength range of 200–800 nm, in which  $\text{BaSO}_4$  was used as the internal reflectance standard. Raman experiments were performed using a DXR spectrometer using the 532 nm laser, and measurements were made in backscattering geometry. Surface electronic states were analyzed on X-ray photoelectron spectroscopy (XPS, PerkinElmer PHI 5300), and the binding energies were referenced to the C1s line at 284.8 eV from adventitious carbon. The photoluminescence (PL) spectra for solid samples were obtained on a F4500 (Hitachi, Japan) photoluminescence detector.

### 2.4. Photoelectrochemical measurement

IPCE (incident photon-to-photocurrent efficiency) measurements were carried out in a CHI 852C electrochemical station with

a solar simulator (Newport 69920, 300 W Xenon lamp), in which the CdSe, CdSe/rGO and  $\text{Ca}^{2+}$ @CdSe/rGO nanoparticles on FTO substrates were used as working electrodes, Ag/AgCl (saturated KCl) as reference electrode, platinum wire as counter electrode, respectively. The working electrode area is in the range of 1 cm<sup>2</sup> with 0.5 M  $\text{Na}_2\text{SO}_4$  solution as a supporting electrolyte. A bias potential of 0.5 V vs. SCE was applied on the photoanode for the photocurrent test under on-off light conditions.

### 2.5. Activity test

The photocatalytic activities of various catalysts were evaluated by the level of photodegradation of TC-HCl with an initial concentration of 15 mg/L TC-HCl solution under visible-light irradiation. Briefly, the photochemical reactor contains 100 mL TC-HCl solution and 0.05 g photocatalysts with recycling water (30 °C) to keep the reactor temperature constant. The reaction solution achieved adsorption and desorption balance after stirring for 30 min in the dark. The photocatalytic reaction was started by irradiating with a 350 W Xenon lamp. Samples were taken from the suspension in 10 min interval and centrifugally separated to remove catalysts for cyclic utilization in additional runs. The concentration of TC-HCl was measured by a UV-vis spectrophotometer at a wavelength of 357 nm.

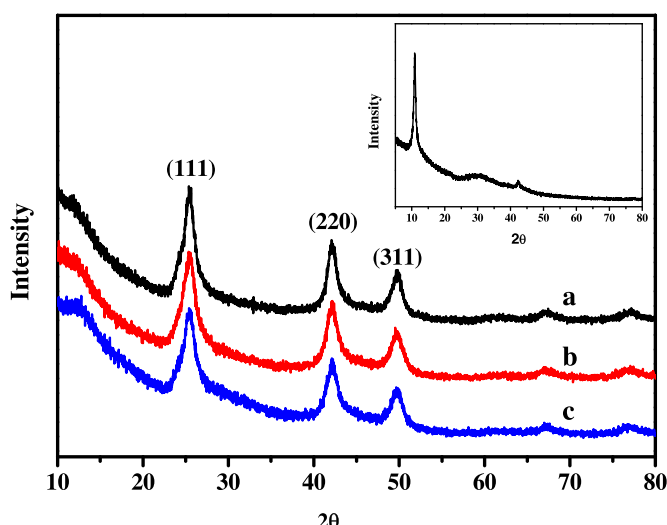


**Fig. 2.** XRD patterns of CdSe (a), CdSe/rGO (b),  $\text{Ca}^{2+}$ @CdSe/rGO (c). The inset is the XRD pattern of GO.

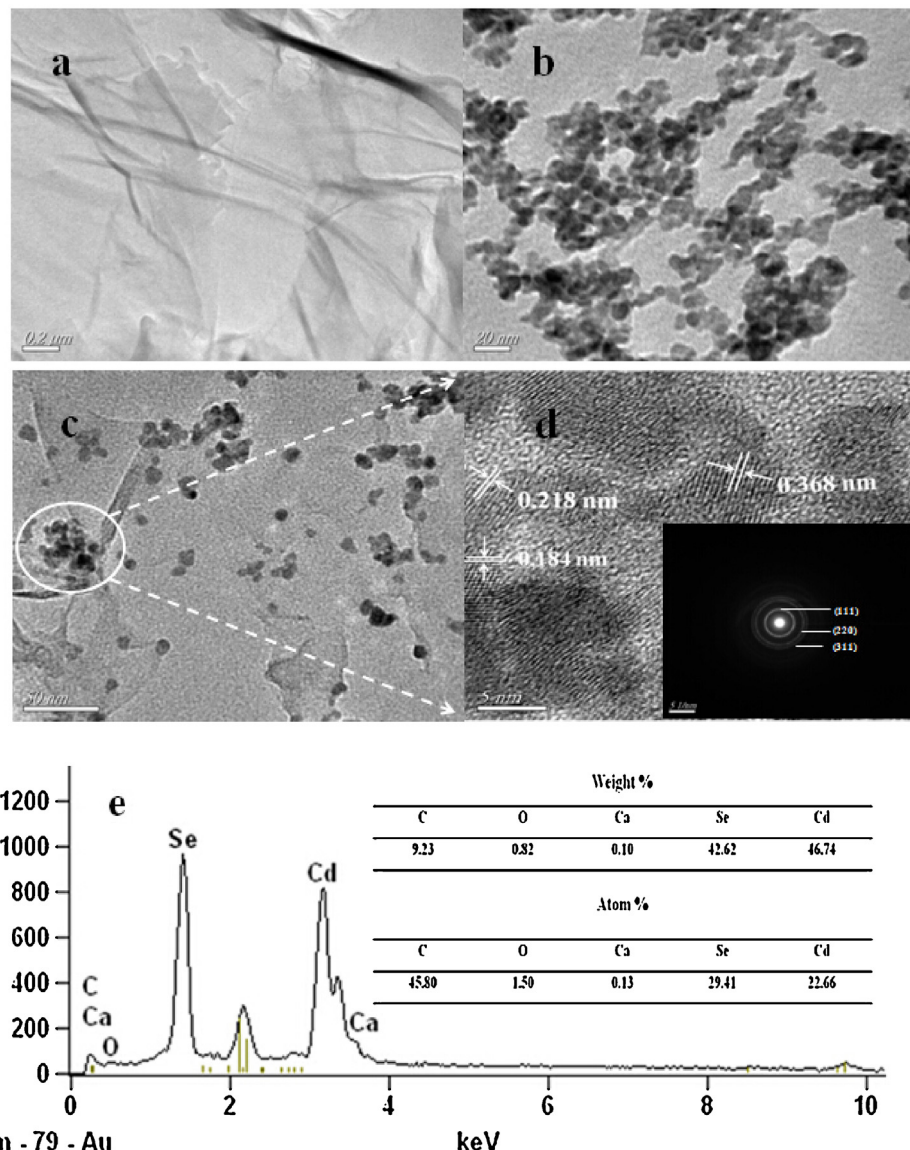


**Fig. 3.** The TEM of GO (a), CdSe QDs (b),  $\text{Ca}^{2+}$ @CdSe/rGO (c), HRTEM image (insert of d SAED patterns) (d), and EDS images of  $\text{Ca}^{2+}$ @CdSe/rGO (e).

### 3. Results and discussion

#### 3.1. Structure and morphology

**Fig. 2** shows XRD patterns of as-prepared photocatalysts CdSe (a), CdSe/rGO (b),  $\text{Ca}^{2+}$ @CdSe/rGO (c). There are no obvious variations according to the patterns. And all of these samples give rise to diffraction peaks of cubic CdSe phase. The diffraction peaks of pure CdSe locating at  $25.4^\circ$ ,  $42.0^\circ$  and  $49.7^\circ$  corresponds to (1 1 1), (2 2 0), and (3 1 1) can be indexed to the cubic phase of CdSe with lattice constant  $6.077\text{\AA}$  (JCPDS 19-0191), respectively. The average crystallite sizes of as-prepared samples calculated from the (1 1 1) peak of XRD pattern by Scherrer formula [33] are about  $9.70\text{ nm}$ ,  $10.78\text{ nm}$  and  $10.41\text{ nm}$ , respectively. Notably, the increase in the crystal size after modification is slightly larger than that pure QDs CdSe, which may be due to the fact that the introduction of rGO can improve crystallinity of CdSe nanoparticles for it providing CdSe an ideal platform for its nucleation [34]. And the ion radius of  $\text{Ca}^{2+}$  ( $0.99\text{\AA}$ ) is just slightly larger than  $\text{Cd}^{2+}$  ( $0.95\text{\AA}$ ) that may be easily entered into CdSe matrix to substitute the  $\text{Cd}^{2+}$  lattice sites, which can also obtain

the nanoparticles with larger sizes after the doping treatment than that of pure CdSe. With a low dopant concentration  $\text{Ca}^{2+}$  (6 mol%), it can be seen that the diffraction peaks are shift to the low degree side instead of appearing new, which indicates that  $\text{Ca}^{2+}$  doped CdSe rather than the mixtures of CaSe and CdSe phases. The crystal structure of QDs CdSe does not show many diversifications after modification. The inset is the XRD pattern of GO, which diffraction peak is located at  $10.3^\circ$ . After hydrothermal reaction, the typical peak belonging to GO is almost invisible. In this study, the diffraction of rGO ( $2\theta = 26^\circ$ ) is nearly without observation in XRD pattern for the low loading content (5 wt%) or the disappearance of the layer-stacking regularity after redox of graphite [35].

#### 3.2. TEM, HRTEM, SAED and EDS images

The morphology and microstructure of GO, CdSe QDs and  $\text{Ca}^{2+}$ @CdSe/rGO are revealed by TEM, HRTEM, SAED and EDS, respectively. **Fig. 3a** shows that the GO is like thin films. From **Fig. 3b**, QDs CdSe is reunion and sphere-like in shape. The main aggregation may be attributed to the as-prepared QDs CdSe with the “small size effect and the surface effect” have more chances to combine

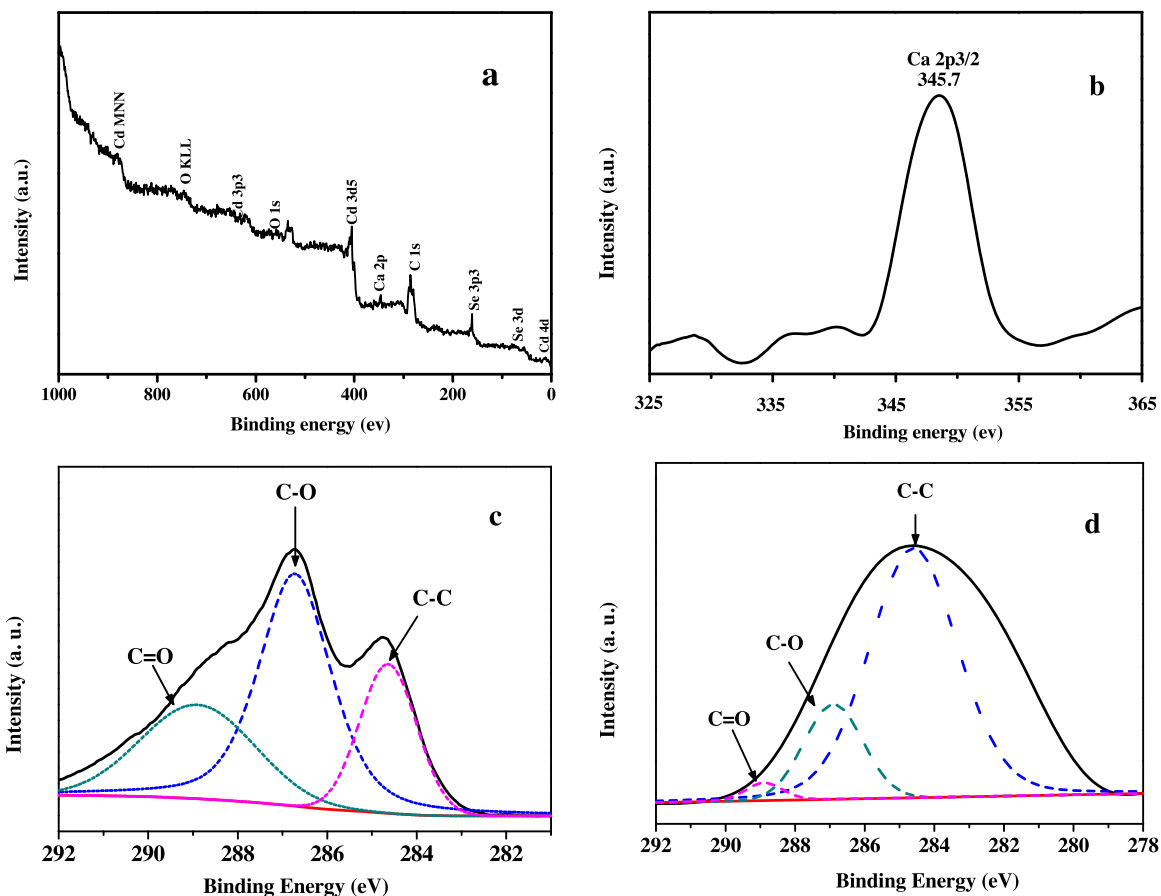


**Fig. 4.** XPS spectrum of the  $\text{Ca}^{2+}$ @CdSe/rGO (a), high resolution scanning XPS of Ca 2p (b), high resolution scanning XPS of C1s of GO (c), and high resolution core level XPS spectrum of C1s of the  $\text{Ca}^{2+}$ @CdSe/rGO nanocomposites (d).

with other atoms. Comparing the morphology of  $\text{Ca}^{2+}$ @CdSe/rGO with CdSe QDs, clearly suggest that the introduction of rGO is of great importance for obtaining a homogeneous distribution of CdSe nanoparticles on rGO sheet. Additionally, assembled particle size becomes smaller with the diameters of about 10 nm, which is in good agreement with the XRD results. There is no apparent aggregation of  $\text{Ca}^{2+}$ @CdSe nanoparticles on the rGO, which may be included that efficient interfacial electric field is established on the interface between rGO and the doped QDs CdSe [36]. The image of high resolution TEM (HRTEM) in Fig. 3d shows the lattice fringe of  $\text{Ca}^{2+}$ @CdSe/rGO sample. Lattice spacings of cubic CdSe are 0.351 nm, 0.215 nm, 0.183 nm corresponding to (1 1 1), (2 2 0) and (3 1 1) planes of cubic CdSe. The lattice fringes of  $\text{Ca}^{2+}$ @CdSe/rGO are detected to be 0.368 nm, 0.218 nm and 0.184 nm, which are slightly larger than the CdSe. The reason may be that the ion radii of  $\text{Ca}^{2+}$  (0.99 Å) is larger than that of  $\text{Cd}^{2+}$  (0.95 Å), which can induce the lattice expansion of CdSe during the doping reaction. The SAED pattern (inset in Fig. 3d) demonstrates that the  $\text{Ca}^{2+}$ @CdSe/rGO nanocomposite possesses crystalline feature of CdSe particles, which is in accordance with the result of XRD analysis. In order to obtain more detailed contents information of the  $\text{Ca}^{2+}$ @CdSe/rGO nanoparticles, EDS spectra from the Fig. 3e give the signals of C, O, Cd, Se, and Ca elements in the composites.

### 3.3. XPS spectra of GO and $\text{Ca}^{2+}$ @CdSe/rGO

In order to further investigate the existence of Ca ion, the elemental state and composition of the  $\text{Ca}^{2+}$ @CdSe/rGO was analyzed by X-ray photoelectron spectroscopy (XPS). Fig. 4a shows the XPS spectra of  $\text{Ca}^{2+}$ @CdSe/rGO, the peaks related to Cd, Se, C, O and

Ca elements. The XPS peak of Ca 2p is illustrated in Fig. 4b. The peaks centered at 345.7 eV correspond to  $\text{Ca}2\text{p}_{3/2}$  [28], indicating that calcium mainly exists  $\text{Ca}^{2+}$ . The XPS results also confirmed the existence of Ca. And the information about removal of oxygenated functional groups from GO after reduction into graphene can also be obtained from XPS spectrum [37]. In the high resolution spectrum of C 1s of GO (Fig. 4c), the peaks at 284.6 eV, 286.7 eV, 288.9 eV correspond to the C–C in the aromatic rings, hydroxyl and C–O epoxy, carbonyl groups, respectively. Fig. 4d shows the XPS spectrum of C 1s of the  $\text{Ca}^{2+}$ @CdSe/rGO. The peak at 284.54 eV of the C–C bond is detected and the other peaks are relatively decreased, which suggests the partly removal of oxygen-containing groups [38].

### 3.4. Raman spectroscopy

Raman spectroscopy has played an important role in studying the bonding properties and defects of graphitic materials. The D band provides information on sp<sup>3</sup> structural defects in carbon, and the stretching of the C–C bond in graphitic materials is ascribed to the G band, which is the typical in-plane vibration of sp<sup>2</sup> bonded carbons [39]. Fig. 5 shows the spectra of GO, CdSe/rGO,  $\text{Ca}^{2+}$ @CdSe/rGO within the range 0–3000 cm<sup>-1</sup>, respectively. Raman spectra in Fig. 5 shows the characteristic D and G bands observed at 1346 and 1587 cm<sup>-1</sup> found in GO, respectively. After hydrothermal treatment, the G bands in Raman spectra of as-prepared CdSe/GO and  $\text{Ca}^{2+}$ @CdSe/GO samples are shifted to the lower frequency side compared to that of GO, which can be attributed to the recovery of the hexagonal network of carbon atoms with defects [37]. The SP2 cluster in the graphene

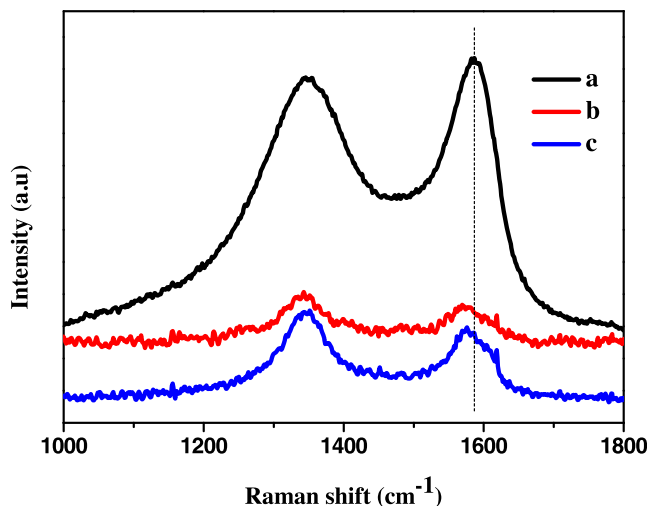


**Fig. 5.** Raman spectra of GO (a), CdSe/GO (b), Ca<sup>2+</sup>@CdSe/GO (c).

materials can be evaluated by I(D)/I(G) ratio. The corresponding I(D)/I(G) ratio of GO, CdSe/rGO, Ca<sup>2+</sup>@CdSe/rGO in Fig. 5 is measured as 0.931, 1.259 and 1.307, respectively. The increasing size of SP2 clusters may be due to the high amount of defects after reaction treatment or remnants GO [37]. We can see obviously from Fig. 5 that intensity of CdSe/rGO and Ca<sup>2+</sup>@CdSe/rGO is smaller than that of GO is due to that the CdSe particles block the Raman signal, since they spread on rGO. We can hardly find out the characteristic Raman peak of CdSe, which may be attributed to the disturbing of strong fluorescence properties in CdSe and the wavelength of the exciting light.

### 3.5. UV-vis DRS

Optical absorption properties and band structure of as-prepared nanomaterials are investigated by UV-vis diffuse reflectance spectra (DRS). The UV-vis absorption spectroscopy of CdSe, CdSe/rGO and Ca<sup>2+</sup>@CdSe/rGO photocatalysts is shown in Fig. 6, respectively. It is widely acknowledged that the photocatalytic activity is closely associated with the light absorption ability. From Fig. 6, all of the as-prepared samples have photo-responses from UV light region to visible light region and show high visible-light absorption ranging from 200 nm to 680 nm, which was consistent with the light

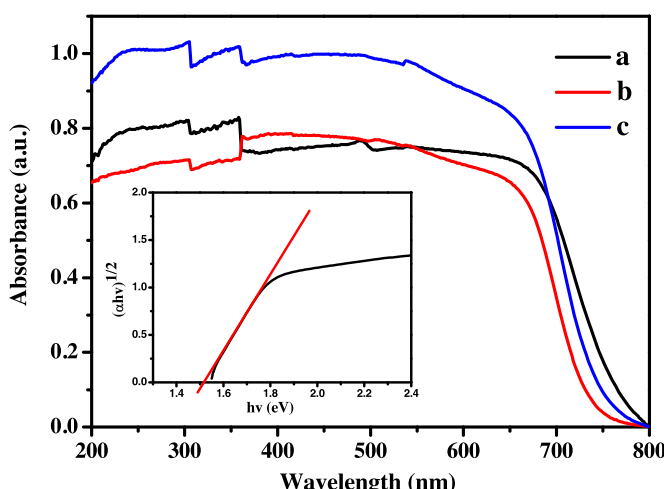


**Fig. 6.** UV-vis absorption spectrum of CdSe (a), CdSe/rGO (b), Ca<sup>2+</sup>@CdSe/rGO (c). The insert is plot of  $[\alpha h\nu]^2$  as a function of photo energy for pure CdSe as an example, which shows how band gap can be obtained.

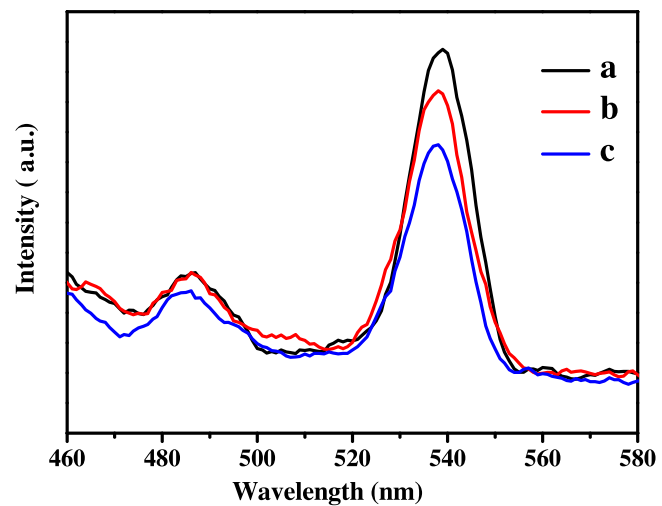


**Fig. 7.** PL spectra of QDs CdSe (a), CdSe/rGO (b) and Ca<sup>2+</sup>@CdSe/rGO (c).

absorbance calculated from the energy band gap. The absorption edge of the CdSe/rGO and Ca<sup>2+</sup>@CdSe/rGO blue shift compares with CdSe, which can be ascribed to the introduction of rGO and Ca<sup>2+</sup>, the electronic interactions and charge equilibration have changed [40]. The optical absorption near the band edge can be calculated by the following Eq. (1) [41]

$$ahv = A(hv - E_g) \quad (1)$$

where  $a$ ,  $v$ ,  $E_g$ , and  $A$  are the absorption coefficient, the light frequency, the band gap, and a constant, respectively. The band gap energy of pure CdSe QDs is about 1.56 eV, which is slightly smaller than 1.75 eV [42] reported in literature, and CdSe/rGO, Ca<sup>2+</sup>@CdSe/rGO is roughly estimated to be 1.59 eV and 1.64 eV, respectively. The band gaps of CdSe/rGO and Ca<sup>2+</sup>@CdSe/rGO are slightly larger than as-prepared CdSe QDs, which can be attributed to the induction of rGO that give rise to the synergistic interaction between semiconductor and rGO support [43]. With a blue shift in the absorbance demonstrates an increase in the band gap than pure CdSe. In addition, the strongest absorption intensity of light for Ca<sup>2+</sup>@CdSe/rGO than the other two nanocomposites indicates that it could obtain the highest photocatalytic activity for a given reaction [30].

### 3.6. PL spectra

It is well acknowledged that the fluorescence intensity of semiconductor is associated with the recombination rate between electron and hole [44]. The stronger fluorescence intensity of the nanomaterial, the higher e<sup>+</sup>/h<sup>-</sup> recombination rate is, which indicates the lower photocatalytic properties of the nanomaterials. Fig. 7 shows PL spectra of the nanomaterials GO (a), CdSe/rGO (b), Ca<sup>2+</sup>@CdSe/rGO (c). The measurement was operated by adding the powder samples in the device covering with a quartz glass in the room temperature under 209.81 nm excitation light source. From Fig. 7, we can see that a strong narrow peak appears at 538.05 nm for QDs CdSe. Compared with the pure QDs CdSe, the PL spectra of CdSe/rGO and Ca<sup>2+</sup>@CdSe/rGO occur blue shift, which can be concluded that after modification with GO and Ca<sup>2+</sup>, the electronegativity of compound nanomaterials enhanced. But the PL emission intensity of Ca<sup>2+</sup>@CdSe/rGO and CdSe/rGO is lower than that of the pure QDs CdSe indicating that the photoexcited electrons have a lower chance for recombination resulting in enhanced visible light activity after the modification. The intensity of Ca<sup>2+</sup>@CdSe/rGO shows lowest, which indicates that this photocatalyst has lower recombination of photo-induced e<sup>+</sup>/h<sup>-</sup> pairs, a longer lifetime of

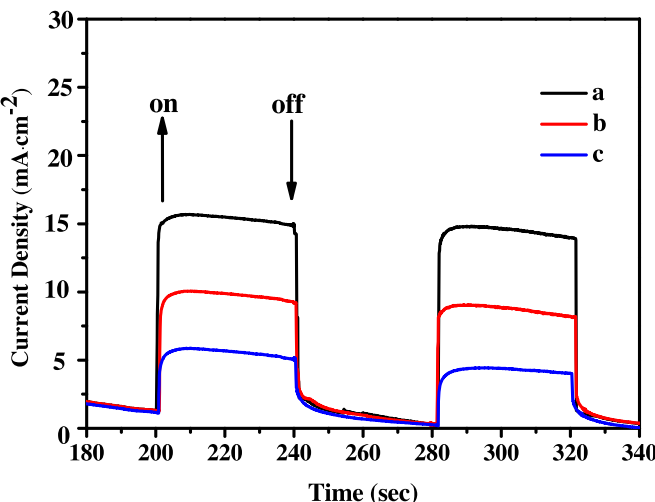


**Fig. 8.** Transient photocurrent response of  $\text{Ca}^{2+}$ @CdSe/rGO (a), CdSe/rGO (b), and CdSe nanocomposite in 0.5 M  $\text{Na}_2\text{SO}_4$  aqueous solution under visible-light irradiation with applied potential of 0.5 V vs.  $\text{Ag}/\text{AgCl}$  (c).

the photogenerated charge carriers and more effectively of the charge carriers migration.

### 3.7. Transient photocurrent response

This prolonged lifetime of the photogenerated charge carriers can also be confirmed by the transient photocurrent responses. Fig. 8 shows the transient photocurrent responses of  $\text{Ca}^{2+}$ @CdSe/rGO (a), CdSe/rGO (b) and CdSe(c) electrodes under intermittent visible-light irradiation and photocurrent densities were measured after using the light on-off process with a pulse of 40 s. It can be seen that CdSe-based nanocomposites with the

introduction of rGO exist significantly enhanced current-potential performance photocurrent toward pure CdSe under visible-light irradiation with applied potential of 0.5 V vs. and the photocurrent decreases to zero as long as the light is switched off. As shown in Fig. 8, among all of the as-prepared nanoparticles,  $\text{Ca}^{2+}$ @CdSe/rGO exhibited the strongest transient photocurrent response. As we all know, the photocurrent is caused by the diffusion of the photogenerated electrons to the back contact, and meanwhile the photoinduced holes are taken up by the hole acceptor in the electrolyte [45,46]. In that case, the strongest photocurrent of  $\text{Ca}^{2+}$ @CdSe/rGO demonstrates the most efficient separation of the photogenerated  $e^-/h^+$  pairs and longest lifetime of the photogenerated charge carriers.

## 3.8. Photocatalytic activity

### 3.8.1. Photocatalytic activity study

Photocatalytic activity of as-prepared catalysts was reflected by photodegrading TC-HCl under visible-light irradiation. The concentration of obtained TC-HCl at various time intervals was investigated by examining the absorption in UV-vis spectra at 357 nm. In order to display the photocatalytic activity of the samples, we prepared, some comparative experiments were conducted under different conditions, and the results are shown in Table 1. And the table also shows the main effect factors of various photocatalyst on photodegrading TC-HCl by presentation the degradation ratio (100%) of different M@CdSe/rGO under visible-light after the adsorption and desorption balance for 30 min in dark. The degradation ratio is calculation from the following expression [47]:

$$\eta = \left( \frac{C_0 - C_t}{C_0} \right) \times 100\% \quad (2)$$

From Table 1, the doped Mg, Ca, Sr, Ba ions with the content of 6 mol%, 6 mol%, 4 mol%, 6 mol% and the loading amount of 5% GO show the highest photocatalytic activity via photodegrading TC-

**Table 1**  
Effect of different doped quantity of M and various copped content of GO on degradation ratio (100%) of tetracycline hydrochloride.

Molar percentage	2 mol%				4 mol%				6 mol%				8 mol%				10 mol%				
	Mg	Ca	Sr	Ba	Mg	Ca	Sr	Ba													
Content of GO	1%	29	35	39	31	33	39	34	30	32	47	63	49	58	63	59	43	49	69	53	62
	3%	55	64	59	61	64	69	70	65	68	81	71	75	63	75	70	69	63	69	71	69
	5%	61	68	74	71	76	79	82	69	79	85	81	83	78	77	80	73	69	74	78	74
	7%	72	68	69	70	76	74	77	65	75	70	79	80	79	75	76	75	72	73	70	71
	9%	62	54	60	52	55	61	53	51	64	61	74	79	67	58	71	68	65	69	53	62

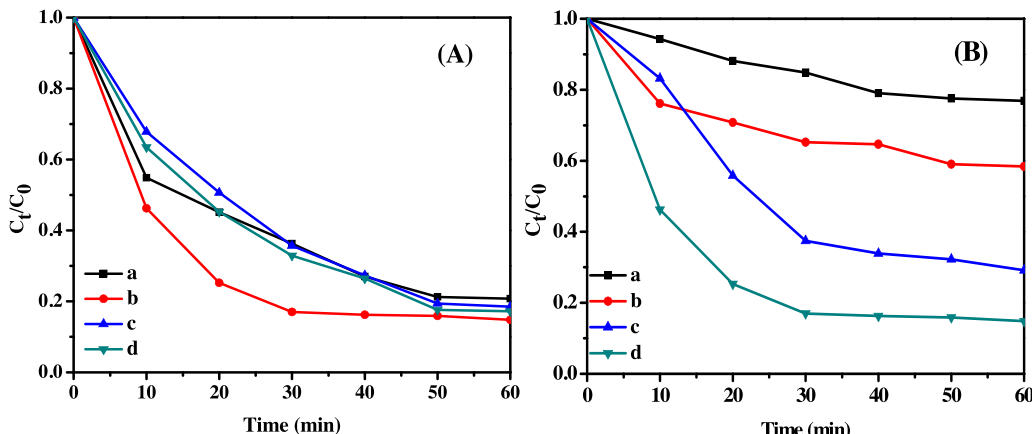


**Fig. 9.** Tetracycline hydrochloride photodegradation efficiency of prepared M@CdSe/rGO (M =  $\text{Mg}^{2+}$  (a),  $\text{Ca}^{2+}$  (b),  $\text{Sr}^{2+}$  (c),  $\text{Ba}^{2+}$  (d)) with optimum value in the doping and loading content (A) and the degradation rate of different targets (CdSe (a), GO (b), CdSe/rGO (c), and  $\text{Ca}^{2+}$ @CdSe/rGO (d)) by photodegradation of tetracycline hydrochloride ( $1.5 \times 10^{-5}$  M, 100 ml) (B).

HCl, respectively. Compared with the various content of doped alkaline earth metal ions, the introduction of rGO has vital impact on photocatalytic activity of catalysts, which may due to the electrons generated in the inorganic semiconductor materials can be transferred to the rGO through the loaded sites under the visible light excitation, and the electrons will participate in the reduction reactions happening on the surface of rGO. At the same time, with the constantly consumed electrons, the photogenerated holes remain on the surface of the prepared materials and participate in oxidation reactions, which efficiently enhance the photocatalytic activity of the samples.

**Fig. 9(A)** illustrates the photocatalytic activity of catalysts with the optimal value in doping and loading, respectively. We can see that, the sample doped with the content of 6 mol%  $\text{Ca}^{2+}$  and 5% GO displays the highest photocatalytic activity compared with the samples doped with Mg, Sr, Ba ions, respectively. The reason may be that the ion radii of  $\text{Ca}^{2+}$  (0.99 Å) is just a bit larger than that of  $\text{Cd}^{2+}$  (0.97 Å) to be more easily embedded into CdSe matrix to replace  $\text{Cd}^{2+}$  lattice sites for the formation of lattice deformation. However, the ion radii of Sr (1.10 Å), Ba (1.30 Å) is too large to enter into the CdSe matrix. And Mg (0.66) is too small to replace  $\text{Cd}^{2+}$ .

**Fig. 9(B)** displays the photo-degradation rate of different photocatalyst by degrading tetracycline hydrochloride. We can clearly see from the figure, the catalytic efficiency is in the order of CdSe < GO < CdSe/rGO <  $\text{Ca}^{2+}$ @CdSe/rGO, which shows that the samples with doped with appropriate amount of Ca ion than the other samples. The reason may be that the opportune doped  $\text{Ca}^{2+}$  can act as a mediator of interfacial to accelerate the electron transfer toward the rGO for participation in the reduction reaction.

### 3.8.2. The intermediates of TC-HCl degradation

The intermediates of TC-HCl were investigated by HPLC-MS and the results were shown in **Fig. 10**. From **Fig. 10**, the deprotonated TC-HCl molecular ion with  $m/z = 445.35$  was found. From the above analysis,  $\text{h}^+$  as the major reactive oxidized species attacked the TC-HCl. The sequence of successive ions fragmentation during collision-induced dissociation was as follows:  $m/z = 445 \rightarrow m/z = 406$  (by loss of OH, H and  $\text{CH}_3$ )  $\rightarrow m/z = 362$  (by loss of  $\text{CONH}_2$ )  $\rightarrow m/z = 318$  (by loss of N,  $\text{CH}_2$  and  $\text{CH}_3$ )  $\rightarrow m/z = 274$  (then by loss of CH, C, H and OH). The processes of the degradation were shown in **Fig. 11**.

### 3.8.3. Stability

Both the photocatalytic efficiency and stability are the important factors to measure the quality of the catalysts. Because of the photocorrosion or photodissolution might occur on the photocatalyst surface in the photocatalytic process. Therefore, we examined the stability of  $\text{Ca}^{2+}$ @CdSe/rGO with the optimum value by photodegrading TC-HCl for four cycles under the same conditions. From **Fig. 12**, the photocatalytic efficiency presents slightly decrease, which could be related to the photocorrosion of the nanoparticles. The difference in crystal structure of as-obtained samples before and after degradation of TC-HCl was compared by examining XRD patterns in **Fig. 13**. It is almost the same in the position of diffraction peaks shown from the figure. The intensity of the figure slightly lower than that before degradation, which may due to the catalyst did not clean thoroughly with residual contamination on the surface or the photocorrosion occurred during the photodegradation process. From the above all, the  $\text{Ca}^{2+}$ @CdSe/rGO exhibited relatively good stability during the photocatalytic reaction.

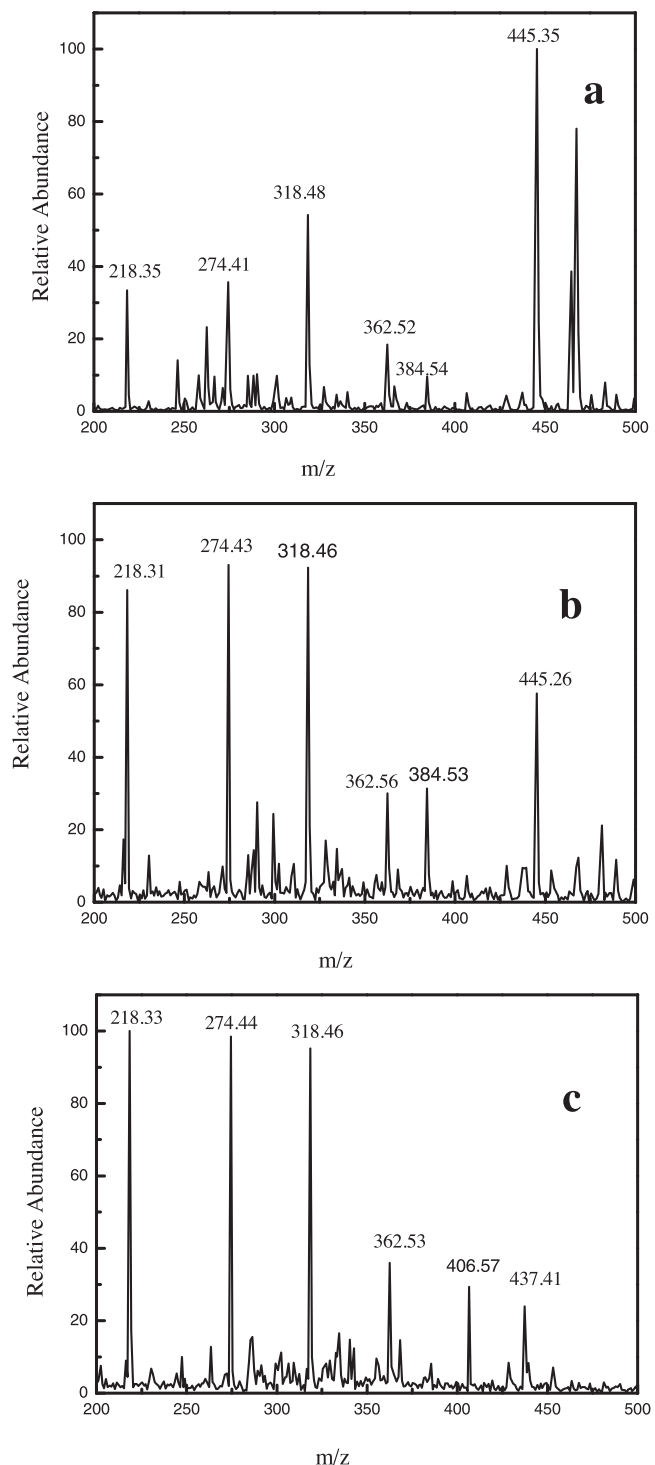


**Fig. 10.** Tetracycline hydrochloride chromatograms and  $m/z$  of degraded tetracycline hydrochloride (a), degradation of tetracycline hydrochloride in 30 min (b), and degradation of tetracycline hydrochloride in 60 min (c).

## 3.9. The mechanism of photo-degradation

### 3.9.1. Active species trapping and $\text{O}_2^{\bullet-}$ , $\text{h}^+$ and $\cdot\text{OH}$ quantification experiments

It has been widely acknowledged that  $\text{O}_2^{\bullet-}$ ,  $\text{h}^+$  and  $\cdot\text{OH}$  are the major factors for the photocatalytic oxidation. **Fig. 14** displays the trapping experiment of active species during the photocatalytic reaction. For investigation of  $\text{O}_2^{\bullet-}$ , the experiment was started by

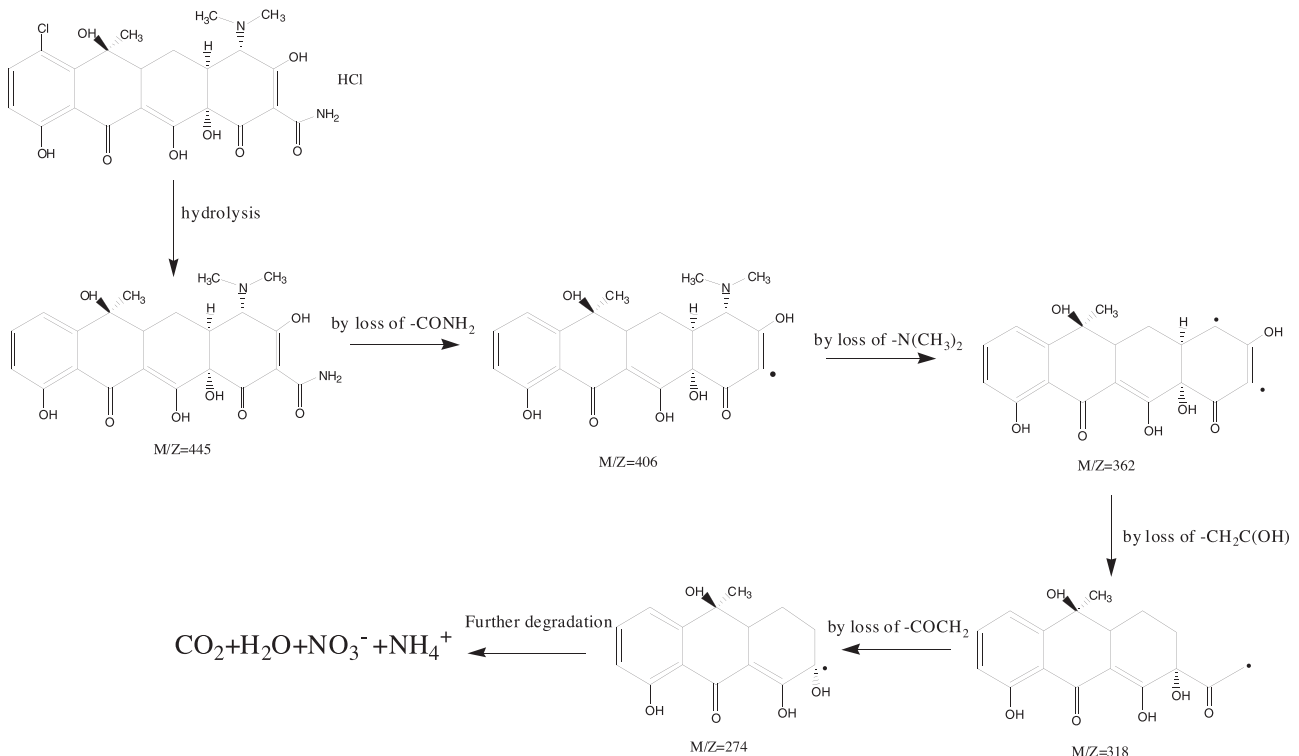


**Fig. 11.** The steps of degradation  $C_{22}H_{25}N_2O_8Cl$  during the photodegrading under visible light.

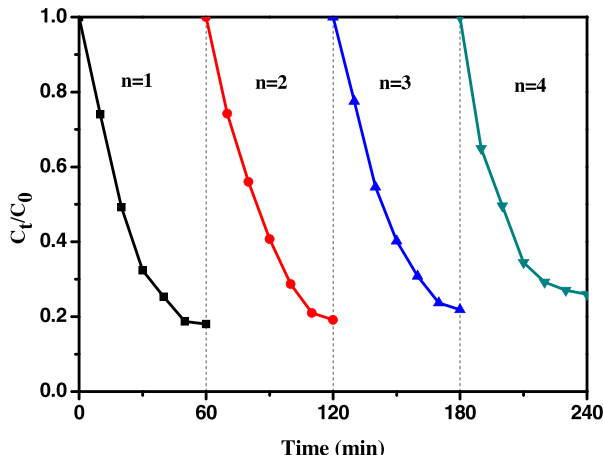


**Fig. 12.** Repeated experiments of photocatalytic degradation of tetracycline hydrochloride by the prepared  $Ca^{2+}@CdSe/rGO$  sample composite with 6 mol%  $Ca^{2+}$  and 5% GO addition.

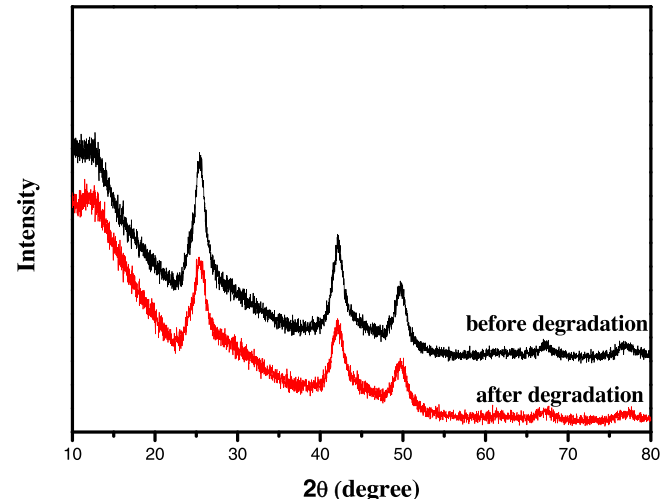


**Fig. 13.** XRD patterns of  $Ca^{2+}@CdSe/rGO$  before tetracycline hydrochloride degradation and after tetracycline hydrochloride degradation for the fourth cycle.

adding 0.5 g/L  $Ca^{2+}@CdSe/rGO$  catalyst and 1 mmol BQ (a quencher of  $O_2^{\bullet-}$ ) for photodegradation 100 mL aqueous solution, and the concentration was measured by a UV-vis spectrophotometer with the maximum absorption wavelength at 357 nm. While for the investigation of  $h^+$  and  $\bullet OH$ , the steps were similar with the procedure of the research of  $O_2^{\bullet-}$ , but adding 1 mmol TEOA (a quencher of  $h^+$ ) and IPA (a quencher of  $\bullet OH$ ) instead of BQ [48], respectively. From the above results, the photocatalytic efficiency of TC-HCl was 85% without adding quencher. With the introduction of TEOA, the photocatalytic efficiency dropped to 19%. However, when the IPA and BQ were added into reaction solution, the degradation efficiencies of TC-HCl were 82% and 75%, respectively. We can see clearly

from the results above,  $h^+$  is the major reactive species during the photocatalytic reaction system for  $Ca^{2+}@CdSe/rGO$  photocatalyst.

### 3.9.2. Proposed mechanisms of the $Ca^{2+}@CdSe/rGO$ photocatalyst

In order to explain the enhanced photocatalytic activity mechanism, the conduction band (CB) and valence band (VB) potentials of CdSe/rGO,  $Ca^{2+}@CdSe/rGO$  should be presented. The CB and VB of as-prepared semiconductors can be calculated via an empirical equation [49]:

$$E_{CB} = X - E_e - 0.5E_g \quad (3)$$

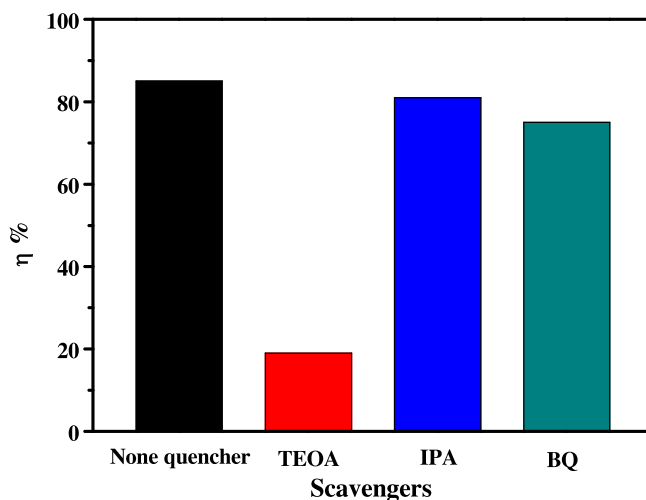


**Fig. 14.** Effects of scavengers and  $\text{Ca}^{2+}$ @CdSe/rGO by adding scavengers on the photocatalytic efficiency of prepared particles.

**Table 2**  
Calculation of CB and VB potentials of CdSe/rGO and  $\text{Ca}^{2+}$ @CdSe/rGO.

	X	$E_g$ (eV)	$E_{CB}$ (eV)	$E_{VB}$ (eV)
CdSe/rGO	0.765	1.59	-0.48	1.11
$\text{Ca}^{2+}$ @CdSe/rGO	0.765	1.64	-0.505	1.135

$$E_{VB} = E_{CB} + E_g \quad (4)$$

where  $E_{CB}$ ,  $E_{VB}$ , X,  $E_g$ ,  $E_e$  are CB edge potential, VB edge potential, electronegativity of the semiconductor, the energy of free electrons on the hydrogen scale (about 4.5 eV) and the band gap energy of the semiconductor, respectively. Based on this calculation, the main values for calculating CB and VB potentials of CdSe/rGO and  $\text{Ca}^{2+}$ @CdSe/rGO are listed in Table 2 [49].

The photocatalytic mechanism schemes of CdSe/rGO and  $\text{Ca}^{2+}$ @CdSe/rGO are shown in Fig. 15. We can see from the figure, the photogenerated electrons ( $e^-$ ) and holes ( $h^+$ ) were produced when the nanoparticles were illuminated by visible light. A lots of electrons ( $e^-$ ) and holes ( $h^+$ ) were generated in CdSe-based materials and the photogenerated electrons ( $e^-$ ) transfer from valence band (VB) to the conduction band (CB) and living holes ( $h^+$ ) in the valence band (VB) [2]. For  $\text{Ca}^{2+}$ @CdSe/rGO system, the photoproduced  $e^-$  to rGO sheet because of the excellent intimate contact

between  $\text{Ca}^{2+}$ @CdSe and rGO, and then takes part in the reduction reaction. However,  $h^+$  on the VB of  $\text{Ca}^{2+}$ @CdSe can not react with  $\text{H}_2\text{O}$  to  $\cdot\text{OH}$  for the  $E_{VB}$  is more negative than  $E(\cdot\text{OH}/\text{OH}^-)$  (2.38 eV vs. NHE) [50], so the photogenerated  $h^+$  takes part in the reduction reaction directly. Of cause, we can see from the figure.  $e^-$  in CB can react with  $\text{O}_2$  to produce  $\cdot\text{O}_2^-$  as the  $E_{CB}$  of  $\text{Ca}^{2+}$ @CdSe (-0.505 eV) is more negative than  $E(\text{O}_2/\cdot\text{O}_2^-)$  (-0.33 V vs. NHE), which can decompose the pollutant. It is in agreement with the result of trapping experiment. While for CdSe/rGO composites, firstly, the  $E_{CB}$  of CdSe (-0.48 eV) is more positive than that of  $\text{Ca}^{2+}$ @CdSe QDs (-0.505 eV) (illustrated in Fig. 15), resulting in much weaker reduction ability of photogenerated electrons. Secondly, the band gap of CdSe/rGO (1.59 eV) is more narrow than that of  $\text{Ca}^{2+}$ @CdSe/rGO, which induces more chance for the recombination reaction of photogenerated  $e^-/h^+$  pairs. This hypothesis can also be confirmed by photocurrent response experiment in Fig. 8.

#### 4. Conclusions

One step hydrothermal method can be successfully applied in the fabrication of earth metal-doped QDs CdSe with different GO additions ( $M = \text{Mg}^{2+}, \text{Ca}^{2+}, \text{Sr}^{2+}, \text{Ba}^{2+}$ ) during which the formation of M doped CdSe nanoparticles and the reduction of GO occur simultaneously. The as-obtained nanoparticles significantly enhance the photocatalytic activities on degrading TC-HCl, which are closely related to the amount of earth metal ions and the induction of rGO. The relatively high photoactivity of  $\text{Ca}^{2+}$ @CdSe/rGO nanocomposites can be attributed to the integrative effect of the enhanced light absorption intensity and the structure and morphology of as-prepared nanomaterials. The possible mechanism for the compounds reveals the effectiveness of interfacial charge transfer, and  $h^+$  is the major reactive species during the photocatalytic reaction system. Overall, the fabricated materials synthesized in one step hydrothermal method and exists high photocatalytic activity which directs our attention to consider the practical application.

#### Acknowledgments

We gratefully acknowledge the financial support of the National Natural Science Foundation of China (No. 21207053, 21407064), the Natural Science Foundation of Jiangsu Province (BK20131259, BK20130489, BK20140532), the Program for Post-graduate Research Innovation in University of Jiangsu Province (No. KYLX1028), and the Research Foundation of Jiangsu University, China (No. 11JDG107).

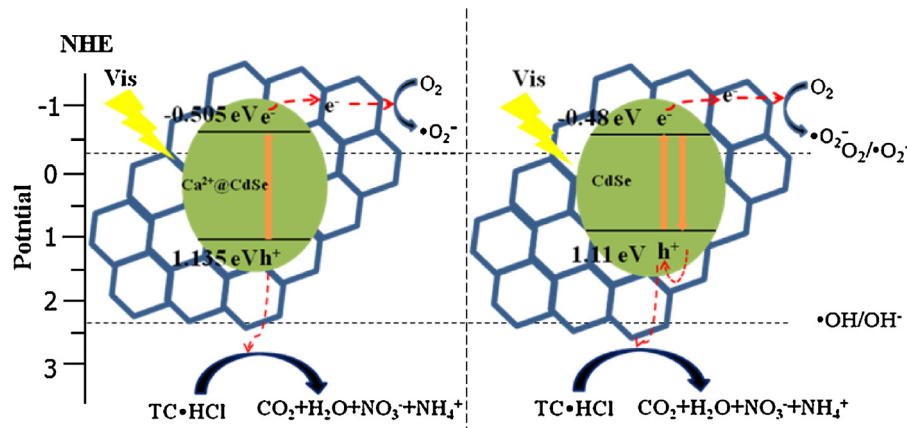


**Fig. 15.** Illustrations of the photo-generated electron transfer process in the  $\text{Ca}^{2+}$ @CdSe/rGO system (left), and QDs CdSe/rGO system (right) under visible light-irradiation.

## References

- [1] L.Q. Ye, J.Y. Liu, C.Q. Gong, L.H. Tian, T.Y. Peng, L. Zan, *ACS Catal.* 2 (2012) 1677–1683.
- [2] S.F. Chen, Y.F. Hu, S.G. Meng, X.L. Fu, *Appl. Catal. B: Environ.* 150–151 (2014) 564–573.
- [3] W.J. Wang, L.Z. Zhang, T.C. An, G.Y. Li, H.Y. Yip, P.K. Wong, *Appl. Catal. B: Environ.* 108–109 (2011) 108–116.
- [4] B.T. Suo, X. Su, J. Wu, D. Chen, A. Wang, Z.H. Guo, *Mater. Chem. Phys.* 119 (2010) 237–242.
- [5] S. Liu, N. Zhang, Z.R. Tang, Y.J. Xu, *ACS Appl. Mater. Interface* 4 (2012) 6378–6385.
- [6] Y.C. Hsiao, T.F. Wu, Y.S. Wang, C.C. Hu, C. Huang, *Appl. Catal. B: Environ.* 148–149 (2014) 250–257.
- [7] Y.Y. Bu, Z.Y. Chen, W.B. Li, B.R. Hou, *ACS Appl. Mater. Interface* 5 (2013) 12361–12368.
- [8] S.Q. Liu, B. Weng, Z.R. Tang, Y.J. Xu, *Nanoscale* 7 (2015) 861–866.
- [9] S. Wang, B.M. Goh, K.K. Manga, Q.L. Bao, P. Yang, K.P. Loh, *ACS Nano* 4 (2010) 6180–6186.
- [10] M.Q. Yang, N. Zhang, M. Pagliaro, Y.J. Xu, *Chem. Soc. Rev.* 43 (2014) 8240–8254.
- [11] X. Zhou, T.J. Shi, H.O. Zhou, *Appl. Surf. Sci.* 258 (2012) 6204–6211.
- [12] Y.H. Zhang, N. Zhang, *Phys. Chem. Chem. Phys.* 14 (2012) 9167–9175.
- [13] S.B. Li, X. Pan, L.K. Wallis, Z.Y. Fan, Z.L. Chen, S.A. Diamond, *Chemosphere* 112 (2014) 62–69.
- [14] N. Zhang, Y.H. Zhang, X.Y. Pan, X.Z. Fu, S.Q. Liu, Y.J. Xu, *J. Phys. Chem. C* 115 (2011) 23501–23511.
- [15] F. Xu, Y.F. Yuan, D.P. Wu, Z. Zhao, Z.Y. Gao, K. Jiang, *Mater. Res. Bull.* 48 (2013) 2066–2070.
- [16] K.M. Hanif, *J. Am. Chem. Soc.* 124 (2002) 11495–11502.
- [17] M. Melvin, D. Kumar, *Superlattices Microstruct.* 58 (2013) 154–164.
- [18] J. Zhao, M.A. Holmes, F.E. Osterloh, *ACS Nano* 7 (2013) 4316–4325.
- [19] X.M. Chen, G.H. Wu, *J. Am. Chem. Soc.* 133 (2011) 3693–3695.
- [20] H.M. Zhu, T.Q. Lian, *J. Am. Chem. Soc.* 134 (2012) 11289–11297.
- [21] N. Zhang, Y. Zhang, Y.J. Xu, *Nanoscale* 19 (2012) 5792–5813.
- [22] D.Q. Zhang, M.C. Wen, S.S. Zhang, P.J. Liu, W. Zhu, G.S. Li, H.X. Li, *Appl. Catal. B: Environ.* 147 (2014) 610–616.
- [23] R. Lotfi, Y. Saboohi, *Physica E* 60 (2014) 104–111.
- [24] K. Ullah, Y.H. Kim, *Chin. Chem. Lett.* 25 (2014) 941–946.
- [25] J.P. Zou, J. Ma, Q. Huang, S.L. Luo, J. Yu, X.B. Luo, W.L. Dai, J. Sum, G.C. Guo, S.L. Suib, *Appl. Catal. B: Environ.* 156–157 (2014) 447–455.
- [26] O.S. Oluwafemi, N. Revaprasadu, *Mater. Lett.* 64 (2010) 1513–1516.
- [27] F. Xu, Y.F. Yuan, *Res. Bull.* 48 (2013) 2066–2070.
- [28] K. Zhang, Z.H. Zhou, L.J. Guo, *J. Hydrogen Energy* 36 (2011) 9469–9478.
- [29] W.S. Hummers, R.E. Offeman, *J. Am. Chem. Soc.* 80 (1958) 1339.
- [30] Y.H. Zhang, Z.R. Tang, X. Fu, Y.J. Xu, *ACS Nano* 4 (2010) 7303–7314.
- [31] A.L. Rogach, A. Kornowski, *J. Phys. Chem. B* 103 (1999) 3065–3069.
- [32] M.Q. Yang, X.Y. Pan, N. Zhang, Y.J. Xu, *CrystEngComm* 15 (2013) 6819–6828.
- [33] K.L. Chung, Y.H. Tsai, *Comput. Math. Appl.* 29 (1995) 109–113.
- [34] S. Lee, K. Lee, W.D. Kim, S. Lee, D.J. Shin, D.C. Lee, *J. Phys. Chem. C* 118 (2014) 23627–23634.
- [35] M.Q. Yang, Y.J. Xu, *Phys. Chem. Chem. Phys.* 15 (2013) 19102–19118.
- [36] H.L. Wang, L.S. Zhang, Z.G. Chen, J.Q. Hu, S.J. Li, Z.H. Wang, J.S. Liu, X.C. Wang, *Chem. Soc. Rev.* 43 (2014) 5234–5244.
- [37] L.M.P. Martinez, S.M. Torres, V. Likodimos, P. Falaras, J.L. Figueiredo, J.L. Faria, A.M.T. Sliva, *Appl. Catal. B: Environ.* 158–159 (2014) 239–340.
- [38] K. Krishnamoorthy, M. Veerapandian, R. Mohan, S.J. Kim, *Appl. Phys. A* 106 (2012) 501–506.
- [39] M.S. Dresselhaus, A. Jorio, M. Hofmann, G. Dresselhaus, R. Saito, *Nano Lett.* 10 (2010) 751–758.
- [40] N.F. Ohtsu, S. Hiromoto, *Surf. Coat. Technol.* 218 (2013) 114–118.
- [41] L.B. Yu, Z. Li, *Appl. Surf. Sci.* 309 (2014) 255–262.
- [42] L.Z. Du, Y. Lei, *Mater. Lett.* 106 (2013) 100–103.
- [43] Z. Chen, N. Zhang, Y.J. Xu, *CrystEngComm* 15 (2013) 3022–3030.
- [44] M.S. Dresselhaus, A. Jorio, M. Hofmann, G. Dresselhaus, R. Saito, *Nano Lett.* 10 (2010) 751–758.
- [45] L. Wu, F. Li, Y.Y. Xu, J.W. Zhang, D.Q. Zhang, G.S. Li, H.X. Li, *Appl. Catal. B: Environ.* 164 (2015) 217–224.
- [46] S. Soedergren, A. Hagfeldt, J. Olsson, S.E. Lindquist, *J. Phys. Chem.* 98 (1994) 5552–5556.
- [47] N. Biswal, K.M. Parid, *Int. J. Hydrogen Energy* 38 (2013) 1267–1277.
- [48] X.L. Liu, Y. Yan, *Chem. Eng. J.* 241 (2014) 243–250.
- [49] L.Q. Ye, J.Y. Liu, C.Q. Gong, L.H. Tian, T.Y. Peng, L. Zan, *ACS Catal.* 2 (2012) 1677–1683.
- [50] P. Wang, D.Z. Li, J. Chen, X.Y. Zhang, J.J. Xian, X. Yang, X.Z. Zheng, X.F. Li, Y. Shao, *Appl. Catal. B: Environ.* 160–161 (2014) 217–226.